

# A Unified Approach to Reliability Assessment of Multiphase DC–DC Converters in Photovoltaic Energy Conversion Systems

Sairaj V. Dhople, *Student Member, IEEE*, Ali Davoudi, *Member, IEEE*,  
Alejandro D. Domínguez-García, *Member, IEEE*, and Patrick L. Chapman, *Senior Member, IEEE*

**Abstract**—A systematic framework for reliability assessment and fault-tolerant design of multiphase dc–dc converters deployed in photovoltaic applications is presented. System-level steady-state models allow a detailed specification of component failure rates, and in turn establish the effects of ambient conditions and converter design on reliability. Markov reliability models are derived to estimate the mean time to system failure. Case studies applied to two- and three-phase, 250-W converters demonstrate that topological redundancy does not necessarily translate to improved reliability for all choices of switching frequency and capacitance. Capacitor voltage rating is found to be the dominant factor that affects system reliability.

**Index Terms**—Markov reliability modeling, maximum power point tracking (MPPT), photovoltaics, switch-mode dc–dc converters.

## I. INTRODUCTION

PHOTOVOLTAIC (PV) systems have gained prominence as economically viable, long-term alternatives to conventional, nonrenewable sources of energy. Power electronic circuits constitute the core of the middleware that processes energy from PV sources in both stand-alone and grid-tied applications. Research in this domain has focused on high-performance, reliable, and cost-effective circuit topologies and control schemes. Maximum power point tracking (MPPT) multiphase dc–dc converters have increasingly been adopted in PV systems, as they offer improved dynamic and steady-state performance with higher reliability when compared to conventional topologies [1], [2]. While only recently considered for PV applications, conventional applications of multiphase converters have included voltage regulator modules [3]–[7], hybrid electric vehicles [8], power factor correction circuits [9], and distributed power supplies [10].

Manuscript received July 12, 2010; revised October 28, 2010; accepted December 10, 2010. Date of current version January 9, 2012. This work was supported by the Grainger Center for Electric Machines and Electromechanics. Recommended for publication by Associate Editor J.-L. Hanen.

S. V. Dhople and A. D. Domínguez-García are with the Department of Electrical and Computer Engineering, University of Illinois at Urbana-Champaign, Urbana, IL 61801 USA (e-mail: sdhople2@illinois.edu).

A. Davoudi is with the Department of Electrical Engineering, University of Texas, Arlington, TX 76019 USA.

P. L. Chapman is with the SolarBridge Technologies, Austin, TX 78758 USA. Color versions of one or more of the figures in this paper are available online at <http://ieeexplore.ieee.org>.

Digital Object Identifier 10.1109/TPEL.2010.2103329

Boost-derived front-end converters are generally favored in PV systems. They offer continuous input current, which reduces input filter requirements and improves dynamic response. Multiphase boost converters with interleaved switching and coupled inductors provide unique advantages in PV applications and have been the subject of extensive research. A coherent state-space averaging method is proposed to analyze a two-phase interleaved boost converter for PV applications in [11]. Interleaved boost converters with strongly coupled inductors demonstrate superior current sharing and small input current ripple in [12]. A prototype of a three-phase, interleaved boost converter with the extremum seeking principle [13] adopted for MPPT is demonstrated in [14].

Conventional multiphase converters with dc inputs are well documented and analyzed [15], [16]. However, generalized analytical models for PV applications have to contend with non-trivial challenges. State-space average models fail to capture the nonlinear, time-varying character of the PV source. Consequently, design choices for analogous converters have not used accurate analytical models, but have rather been based on expected behavioral norms.

Reliability of PV energy conversion systems is very important owing to the typically high fixed costs. Inclusive and detailed reliability models are available for PV modules [17], [18]. In particular, Petrone *et al.* [19] (and related references within) demonstrated that PV modules are among the most reliable components in the energy conversion chain. Therefore, recent study on system reliability has addressed the power electronic circuits that process PV energy. Practical considerations for balance-of-system components are well detailed in [20]. A systematic reliability assessment approach for power electronics components in PV systems is demonstrated in [21]. Derated semiconductor devices allow construction of more reliable converters without resorting to soft-switching techniques in [22]. Chan *et al.* [23], [24] examined the reliability of different PV circuit topologies. Results indicate that the switching stage is most likely to fail and temperature is revealed as the most likely cause of failure. Emerging concerns associated with the reliability of anti-islanding techniques and MPPT algorithms are addressed in [19]. The growth in residential and commercial grid-tied PV systems [25]–[27] has renewed focus on the reliability of grid-tied inverters [28], [29].

We have proposed analytical, steady-state models in [30] to accurately and rapidly describe the operation of multiphase boost converters over a wide range of ambient conditions. A

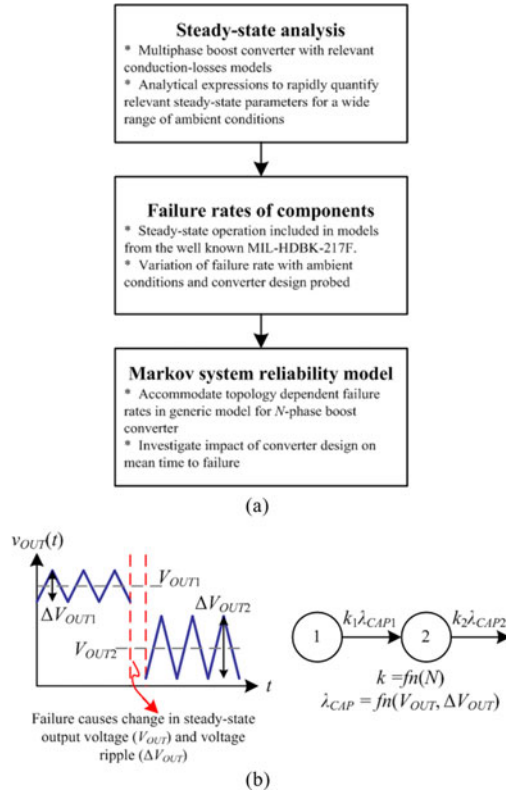


Fig. 1. (a) Proposed analysis technique (b) handles topology-dependent failure rates with device failure.

systematic framework for reliability assessment is consequently set forth in [31], as the steady-state models enable a detailed specification of converter component stresses. The goal of this paper is to integrate analytical tools for assessing converter performance set forth in [30], with system reliability Markov-based models developed in [31] in a unified manner. The suggested approach minimizes the subjectivity introduced in current reliability evaluation techniques. Rather than using a qualitative description of the system's functionality, this methodology uses system steady-state behavior to completely specify component failure rates. Reliability-related evaluations are based on the quantitative analysis of system performance considering all possible component failures and the sequence of failure. This minimizes the ambiguity that tends to arise when using qualitative models of the system's functionality to formulate the system reliability model. It is important to note that this methodology integrates circuit performance and stochastic behavior due to component failures, as the system reliability model generated is clearly dependent on steady-state performance. The block diagram shown in Fig. 1(a) summarizes the proposed approach to reliability analysis. Fig. 1(b) depicts a hypothetical situation where a failure in the circuit changes the steady-state operation and modifies the device failure rates. The ability of the proposed reliability assessment technique to handle such situations is examined in detail as follows.

The contributions of this study are outlined as follows.

- 1) The proposed unified approach to reliability assessment provides a systematic alternative to conventional design

approaches based on empirically accepted system-level traits.

- 2) The converter's steady-state operation undeniably affects the system reliability. For instance, consider the hypothetical situation shown in Fig. 1(b), where a failure in some circuit component causes a change in the output voltage ( $V_{OUT}$ ) and output voltage ripple ( $\Delta V_{OUT}$ ). The failure rate of the filter capacitors is dependent on the output voltage and output voltage ripple (24). Hence, a topological change, as shown in the figure, modifies the capacitor failure rate from  $k_1 \lambda_{CAP1}$  to  $k_2 \lambda_{CAP2}$ . Therefore, it is imperative to consider both parameters such as the voltage ripple imposed on capacitors and power losses in switching devices, and the dependence of failure rates on circuit topology. As depicted in the block diagram in Fig. 1(a), this study addresses the impact of converter steady-state performance and circuit topology on device failure. This provides the circuit designer with a framework to seamlessly integrate reliability into performance-oriented design.
- 3) A thorough steady-state analysis for MPPT implemented with a fairly involved multiphase topology is provided. The analytical models derived include the effect of losses in the switching and energy storage elements. Past study on MPPT converters has typically neglected converter losses.
- 4) The proposed steady-state characterization and subsequent reliability analysis is verified through case studies applied to a multiphase boost converter.

The remainder of this paper is organized as follows. Models of the PV module, converter, and MPPT controller are presented in Section II. Steady-state operation of a generic  $N$ -phase converter is addressed in Section III. In Section IV, the impact of ambient conditions and converter design on the failure rates of the components is assessed. Finally, in Section V, Markov reliability models are derived to estimate the converter's mean time to failure (MTTF). This allows us to quantify the impact of circuit parasitics and other design choices, such as switching frequency and component voltage ratings on system reliability.

## II. PV MODULE, MULTIPHASE CONVERTER, AND MPPT CONTROLLER MODELS

This section describes the behavioral model used to describe the PV module. Models of the multiphase converter with interleaved switching, and the MPPT control scheme based on ripple correlation control (RCC) are also presented.

### A. PV Module Model

A physics-based model of a solar cell is shown in Fig. 2 [32]–[34]. The current sourced ( $I_{SC}$ ) is proportional to the incident insolation. The diode parameters and series and shunt resistances ( $R_S$  and  $R_P$ , respectively) are functions of the fabrication process. Fig. 3 depicts a conventional PV module with several cells connected in series to augment the module voltage.

In practice, it is difficult to obtain parameters to accurately model individual solar cells. Data sheets of PV modules

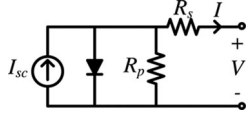


Fig. 2. Solar cell model.

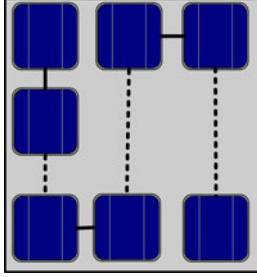


Fig. 3. Layout of cells in PV module.

typically do not provide detailed information about the parameters of the solar cells or their layout in the module. To circumvent these impediments, Jianhui *et al.* [35] proposed the following description for the PV module current  $I$  as a function of terminal voltage  $V$ :

$$\begin{cases} I = I_{SC} [1 - C_1 (e^{V/C_2 V_{OC}} - 1)] \\ C_1 = \left(1 - \frac{I_M}{I_{SC}}\right) e^{(-V_M/C_2 V_{OC})} \\ C_2 = \frac{(V_M/V_{OC}) - 1}{\ln[1 - (I_M/I_{SC})]} \end{cases} \quad (1)$$

where subscripts “ $M$ ,” “ $OC$ ,” and “ $SC$ ” refer to maximum power point (MPP), open circuit, and short circuit, respectively. The parameters in (1) are readily available in data sheets of PV modules. For completeness, these quantities are corrected for solar insolation and ambient temperatures that differ from standard test condition (STC) values of  $1000 \text{ W/m}^2$  and  $25^\circ\text{C}$ , respectively, in the following equations [35]:

$$\Delta T = T - T_{STC} \quad (2)$$

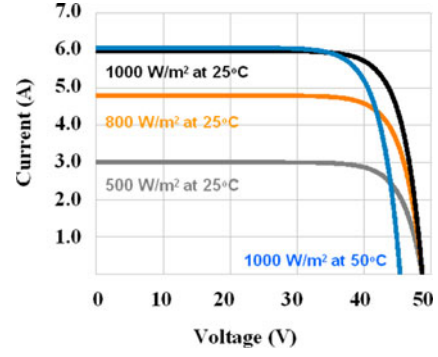
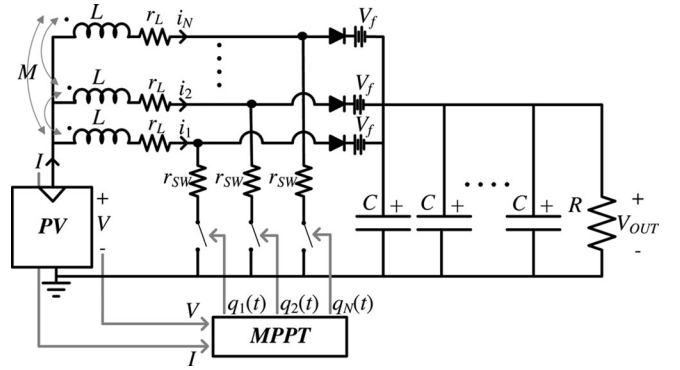
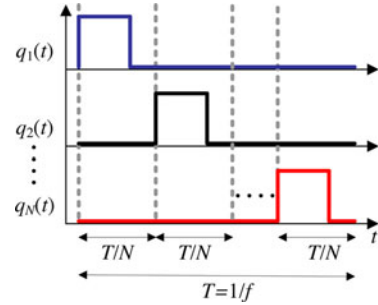
$$I_{SC} = I_{SC-STC} \left( \frac{S}{S_{STC}} \right) + \alpha \Delta T \quad (3)$$

$$I_M = I_{M-STC} \left( \frac{S}{S_{STC}} \right) + \alpha \Delta T \quad (4)$$

$$V_{OC} = (V_{OC-STC} - \beta \Delta T) \quad (5)$$

$$V_M = (V_{M-STC} - \beta \Delta T). \quad (6)$$

For illustration, the 230-W, SPR-230-WHT PV module is adopted here [36]. Relevant parameters of the module are sum-


 Fig. 4. Simulated  $I$ - $V$  curves of SPR-230-WHT module.

 Fig. 5.  $N$ -phase, interleaved boost converter model.

 Fig. 6. Interleaved switching scheme for  $N$ -phase converter.

marized in Appendix A. Fig. 4 shows the  $I$ - $V$  characteristic of the module, as extracted from the model described.

### B. Multiphase Interleaved Boost Converter

Fig. 5 depicts the  $N$ -phase converter model analyzed. The model accounts for common conduction losses, including resistive losses in the switching devices ( $r_{SW}$ ), copper losses in the coupled inductor ( $r_L$ ), and forward voltage drops of the diodes ( $V_f$ ). The interleaved switching scheme is illustrated for the  $N$ -phase converter in Fig. 6. The switching commands  $q_i(t)$  are out of phase by  $(2\pi/N)$  rad over a switching period  $T$ . The switch

states are determined by an MPPT algorithm, described in the following section.

To simplify the forthcoming analysis, it is assumed that each phase is equally coupled with every other phase. Hence, the inductance matrix  $\mathbf{L}$  has the following structure:

$$\mathbf{L} = \begin{bmatrix} L & M & \dots & M \\ M & L & \dots & M \\ \dots & \dots & \dots & \dots \\ M & M & \dots & L \end{bmatrix}_{N \times N} \quad (7)$$

where the self and mutual inductances in the  $N$ -winding coupled inductor are denoted as  $L$  and  $M$ , respectively. Losses due to saturation and eddy currents are disregarded. In the proposed application, a relatively low switching frequency is utilized, which renders copper loss more dominant when compared to core loss. Additionally, it is assumed that the magnetic design avoids saturation under all operating conditions.

### C. Ripple Correlation Control (RCC)

Innumerable techniques to track the MPP of a PV array are documented in the literature (see [37]–[40] and references within for recent work in this area). Here, MPPT is implemented using RCC [41], [42]. RCC utilizes voltage and current ripple, inherently present in switch-mode power converters, to maximize the power from a PV array. The algorithm is inherently robust and offers simple analog hardware implementation. For a boost converter, the RCC law for the duty cycle is expressed as

$$d_{\text{SW}}(t) = -k \int \left( \frac{dp}{d\tau} \right) \left( \frac{dv}{d\tau} \right) d\tau \quad (8)$$

where,  $d_{\text{SW}}(t)$  refers to the duty-cycle command, which is compared to a ramp signal to generate the switching signal  $q(t)$ . The PV module power and voltage are denoted as  $p$  and  $v$ , respectively, and  $k$  is a positive constant. As the coupled inductors in the multiphase converter ensure current sharing [10], the same duty-cycle command can be used to control every phase. An outer current-balancing loop can be adopted as in [12] to ensure that the phase currents are balanced. For further information on current balancing in multiphase converters, refer [43]–[45].

## III. STEADY-STATE OPERATION OF $N$ -PHASE CONVERTER

Analytical, closed-form expressions to capture the output voltage, duty cycle, and peak-to-peak output voltage ripple in a generic  $N$ -phase converter controlled for MPPT are derived here. These expressions enable rapid evaluation of the stresses imposed on different components and are subsequently employed in the reliability analysis.

### A. Output Voltage

In steady state, the MPPT controller ensures that the terminal voltage and module current are the MPP values  $V_M$  and  $I_M$ , respectively. Imposing charge-second balance for the output

capacitors

$$N \int_{D_D T} \left( i(t) - \frac{V_{\text{OUT}}}{R} \right) dt + N \int_{D_{\text{SW}} T} -\frac{V_{\text{OUT}}}{R} dt = 0. \quad (9)$$

This implies

$$\left( I_M - \frac{V_{\text{OUT}}}{R} \right) D_D - \left( \frac{V_{\text{OUT}}}{R} \right) D_{\text{SW}} = 0. \quad (10)$$

The duty cycles of the active switch  $D_{\text{SW}}$  and diode  $D_D$  for an  $N$ -phase converter are related as follows:

$$D_{\text{SW}} + D_D = \frac{1}{N}. \quad (11)$$

Also, the power balance in the circuit implies the following:

$$P_{\text{IN}} = P_{\text{OUT}} + P_{\text{LOSS}} \quad (12)$$

$$V_M I_M = \frac{V_{\text{OUT}}^2}{R} + P_L + P_{\text{SW}} + P_D. \quad (13)$$

Circuit losses are the sum of the copper loss in the coupled inductors  $P_L$ , resistive losses in the switches  $P_{\text{SW}}$ , and losses due to the forward voltage drop of the diodes  $P_D$ . Given the assumptions of strong coupling and sufficiently large self inductance, each individual phase carries the entire PV current  $I_M$ , when either the active switch or diode conduct. Otherwise, the phase current is zero. Based on this observation, the losses are substituted in (13) to yield the following:

$$V_M I_M = \frac{V_{\text{OUT}}^2}{R} + I_M^2 r_L + N I_M^2 r_{\text{SW}} D_{\text{SW}} + N I_M V_f D_D. \quad (14)$$

Substituting for  $V_{\text{OUT}}$  from (10) and  $D_D$  from (11) in (14) yields the following quadratic equation in the duty ratio  $D_{\text{SW}}$ :

$$D_{\text{SW}}^2 [N^2 I_M^2 R] + D_{\text{SW}} [N I_M^2 r_{\text{SW}} - N I_M V_f - 2 N I_M^2 R] + [I_M^2 R - I_M V + I_M^2 r_L + I_M V_f] = 0 \quad (15)$$

Equation (15) yields two values of  $D_{\text{SW}}$ . The solution greater than 50% is neglected given the knowledge of converter operation (11). Equation (10) then provides the following expression for the output voltage:

$$V_{\text{OUT}} = I_M R (1 - D_{\text{SW}} N) \quad (16)$$

### B. Output Voltage Ripple

Consider the current through the capacitor bank, composed of  $N$  capacitors, each with capacitance  $C$

$$i_C(t) = N C (dv_{\text{OUT}}/dt). \quad (17)$$

Approximating the capacitor current during the period  $D_D T$  with a straight-line fit for the output voltage provides the expression in (18), where the current through the capacitor bank is approximated as the difference between the PV current  $I_M$  and the load current as follows:

$$I_M - \frac{V_{\text{OUT}}}{R} = N C \frac{\Delta V_{\text{OUT}}}{D_D T}. \quad (18)$$

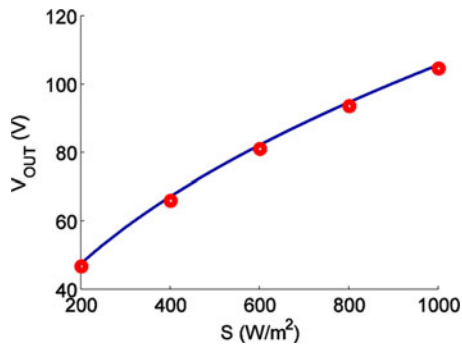


Fig. 7. Output voltage as a function of insolation at 25 °C.

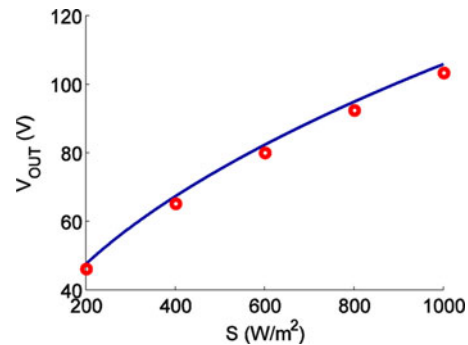


Fig. 8. Output voltage as a function of insolation at 50 °C.

Isolating the output voltage ripple

$$\Delta V_{\text{OUT}} = \left( I_M - \frac{V_{\text{OUT}}}{R} \right) \frac{D_D T}{NC}. \quad (19)$$

### C. Power Losses

The following expressions capture the power losses in the coupled inductor  $P_L$ , switches  $P_{\text{SW}}$ , and diodes  $P_D$ :

$$P_L = I_M^2 r_L \quad (20)$$

$$P_{\text{SW}} = N I_M^2 r_{\text{SW}} D_{\text{SW}} \quad (21)$$

$$P_D = N I_M V_f D_D. \quad (22)$$

The winding and switch resistances in the inductors and switches, respectively, are denoted as  $r_L$  and  $r_{\text{SW}}$ . The forward voltage drop of the diodes is denoted as  $V_f$ .

Other losses can easily be incorporated into the analysis through (13). For example, a detailed model could include switching and commutation losses, eddy currents, and hysteresis losses in the magnetics. While interesting design tradeoffs can be envisioned with more detailed models, the focus of this study is to set forth a reliability assessment framework that can easily be adapted to such specific applications.

A three-phase converter, with specifications listed in Table II (see Appendix B) and the PV module described in Table I (see Appendix A), is employed to validate the analytical, steady-state model. The model is verified over the insolation range 200–1000 W/m<sup>2</sup> at ambient temperatures of 25 °C and 50 °C. Results are shown in Figs. 7–12. In each case, the results from the analytical models are plotted as continuous lines (–), and the data points extracted from the detailed, switch-level simulations are shown as circles (○). The analytical models developed for the converter accurately describe the steady-state operation over a wide range of ambient conditions. The percentage error is no more than 3% for the output voltage, and no more than 7% for the output voltage ripple. The maximum difference in the predicted and measured duty cycle is less than 2%.

Operational stresses on the components can be assessed from expressions derived above for the output voltage, peak-to-peak output voltage ripple, power losses, and duty cycles of the active switches and diodes. In the forthcoming section, these stresses are employed to describe component failure rates used in the Markov reliability model.

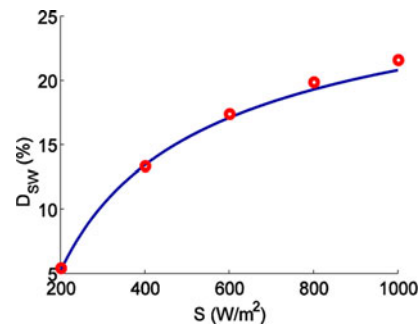


Fig. 9. Duty cycle as a function of insolation at 25 °C.

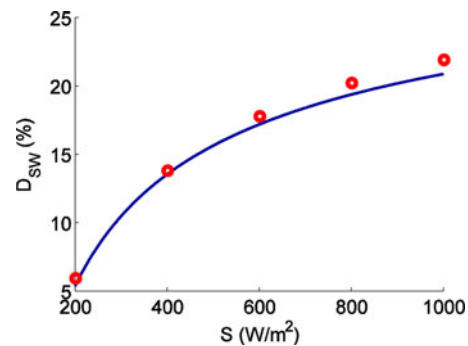


Fig. 10. Duty cycle as a function of insolation at 50 °C.

## IV. FAILURE RATES OF COMPONENTS IN N-PHASE CONVERTER

The failure-rate models in this paper are adopted from the *Military Handbook for Reliability Prediction of Electronic Equipment*, MIL-HDBK-217 F [46]. The models prescribed by [46] have been criticized as pessimistic [21], and updated failure-rate models are available [47]. However, we employ [46] as it provides an extensive database of components and serves as a unified source for failure-rate models. Additionally, the focus of this work is to provide a framework for reliability-focused design, and as such, any available source of failure-rate models can be adopted in the outlined analytical procedure.

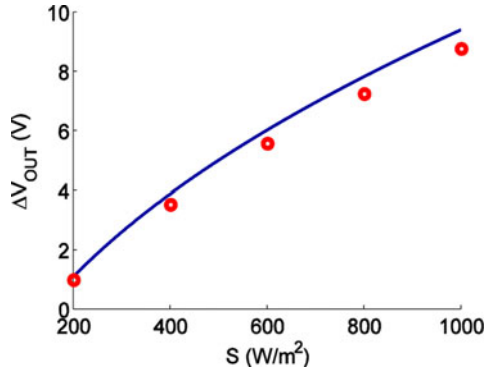


Fig. 11. Output voltage ripple as a function of insolation at 25 °C.

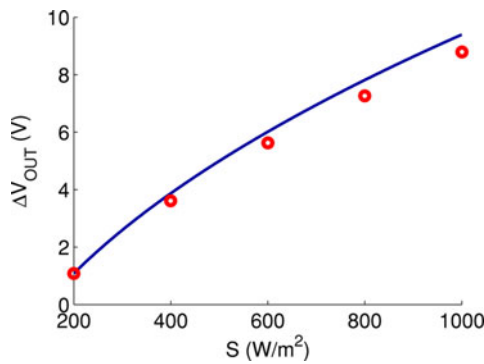


Fig. 12. Output voltage ripple as a function of insolation at 50 °C.

The time-invariant rates proposed in [46] are of the general form in the following equation and correspond to exponentially distributed component lifetimes

$$\lambda_P = \lambda_B \pi_E \pi_Q \prod_i \pi_i. \quad (23)$$

In (23), the failure rate  $\lambda_B$  is the base failure rate and  $\pi_E$  and  $\pi_Q$  are modifiers to account for environmental and qualitative effects. Other device-specific modifiers are denoted as  $\pi_i$ . All failure rates in [46] are expressed with units of failures per million hours of operation.

Failure rates of the different components in the multiphase converter are described in this section. For each component, the effect of ambient conditions, device ratings, and number of phases is probed through case studies applicable to converter specifications listed in Table II, and PV module specifications listed in Table I. This provides a useful starting point to assess the overall reliability of an  $N$ -phase converter.

#### A. Capacitor

Dry electrolytic aluminum capacitors are used as the output stage of the converter. The failure rate of the capacitors  $\lambda_{CAP}$  is

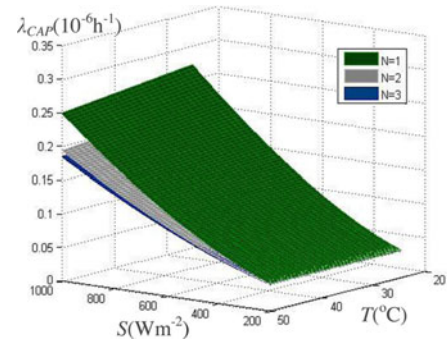


Fig. 13. Capacitor failure rate as a function of number of phases.

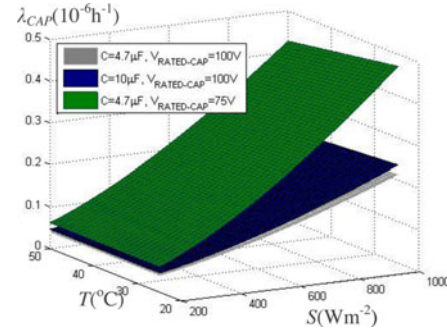


Fig. 14. Capacitor failure rate as a function of capacitance and voltage.

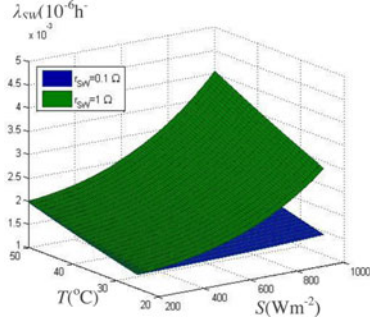
expressed as follows:

$$\begin{cases} \lambda_{CAP} = \lambda_B \pi_{CV} \pi_E \pi_Q \\ \lambda_B = 0.0028 \left[ \left( \frac{S_{CAP}}{0.55} \right)^3 + 1 \right] \exp \left( 4.09 \left( \frac{T + 273 \text{ K}}{358 \text{ K}} \right)^{5.9} \right) \\ S_{CAP} = \frac{V_{OUT} + (\Delta V_{OUT}/2)}{V_{RATED-CAP}} \\ \pi_{CV} = 0.32 (C \mu\text{F})^{0.19}. \end{cases} \quad (24)$$

The operational voltage stress  $S_{CAP}$  is defined as the ratio of the peak-to-rated capacitor voltage. The capacitance factor  $\pi_{CV}$  derates the failure rate based on the value of capacitance in microfarad  $C$ . Finally,  $\pi_E$  and  $\pi_Q$  are 2 and 10, respectively, for ground-based applications and nonmilitary-grade capacitors. Fig. 13 depicts the variation of the capacitor failure rate  $\lambda_{CAP}$  as a function of incident insolation  $S$  and ambient temperature  $T$  for different phase numbers  $N$ . As  $N$  increases, the output voltage ripple decreases, and hence, the failure rates drop across all ambient conditions. Also, the influence of insolation is dominant compared to temperature.

The impact of voltage rating and capacitance is demonstrated in Fig. 14. While  $\lambda_{CAP}$  increases with higher capacitance because of the capacitance factor, it decreases with an increase in voltage rating, which guarantees a lower voltage stress (24).

The choice of capacitor technology is critical to the system reliability. The choice of electrolytic capacitors is purely for illustrative purposes. Failure-rate models for other technologies are available in [46] and can be incorporated into the analysis for comparing different technologies. For more information on

Fig. 15. Switch failure rate as a function of  $r_{SW}$ .

the impact of capacitor technology on reliability, refer to [27] and [48].

### B. Active switch

$N$ -channel silicon-power field-effect transistors are used in the converter, and their failure rate is described as follows:

$$\begin{cases} \lambda_{SW} = \lambda_B \pi_T \pi_A \pi_E \pi_Q \\ \pi_T = \exp \left[ -1925 \text{ K} \left( \frac{1}{T_J + 273 \text{ K}} - \frac{1}{298 \text{ K}} \right) \right] \\ T_J = T_C + \Theta_{JC} P_{SW}. \end{cases} \quad (25)$$

The base failure rate  $\lambda_B$  is constant and equal to 0.012. The junction temperature  $T_J$  is the sum of the case temperature  $T_C$  and the product of the junction–case thermal resistance  $\Theta_{JC}$  and switch power loss  $P_{SW}$ . More information on this thermal model and guidelines to estimate the thermal resistance, and device case temperature are provided in [46]. The application and quality factors  $\pi_A$  and  $\pi_Q$  are 8 (for switches rated at 200 W). The conduction losses in the switch severely impair reliability. This is illustrated in Fig. 15, which depicts the variation of the switch failure rate  $\lambda_{SW}$  with switch resistance  $r_{SW}$ .

### C. Diode

The failure rate of the Schottky power diodes employed in the converter is expressed as follows:

$$\begin{cases} \lambda_{DIODE} = \lambda_B \pi_T \pi_S \pi_C \pi_E \pi_Q \\ \pi_T = \exp \left[ -3091 \text{ K} \left( \frac{1}{T_J + 273 \text{ K}} - \frac{1}{298 \text{ K}} \right) \right]. \end{cases} \quad (26)$$

The base failure rate  $\lambda_B$  is constant and equal to 0.003 for Schottky devices. The temperature factor  $\pi_T$  depends on the junction–case temperature, which is computed in the same way as for the active switch (25). The stress factor  $\pi_S$  accounts for the operational reverse-voltage stress of the diode relative to the rated voltage as follows:

$$\pi_S = \begin{cases} \left( \frac{V_{OUT}}{V_{RATED-DIODE}} \right)^{2.43}, & \text{for } 0.3 < \left( \frac{V_{OUT}}{V_{RATED-DIODE}} \right) \leq 1 \\ 0.054, & \text{for } \left( \frac{V_{OUT}}{V_{RATED-DIODE}} \right) \leq 0.3. \end{cases} \quad (27)$$

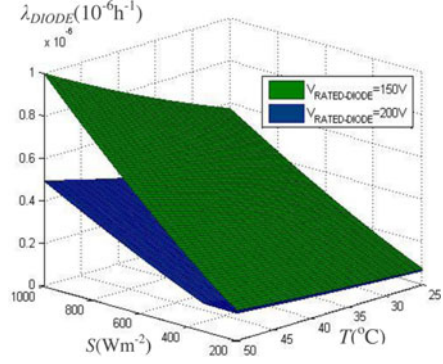


Fig. 16. Diode failure rate as a function of the diode-voltage rating.

The effect of the diode physical contact with the printed circuit board is captured by the contact construction factor  $\pi_C$ . This factor is unity for metallurgical bonded contacts. Similar to the active switch,  $\pi_Q$  is set to 8.

The variation of diode failure rate  $\lambda_{DIODE}$  with voltage rating  $V_{RATING-DIODE}$  is depicted in Fig. 16. Apart from the obvious improvement in reliability with the increased voltage rating,  $\lambda_{DIODE}$  is more sensitive to temperature as compared to  $\lambda_{CAP}$ . Additionally, for a given insolation,  $\lambda_{CAP}$  is inversely proportional to temperature, while  $\lambda_{DIODE}$  is directly proportional.

The failure rate of the inductors is a function of ambient temperature and independent of converter design (e.g., number of phases and switching frequency). Additionally, over a given range of ambient conditions, the failure rate of the inductors is likely to be lower than the other components in the converter. Hence, we disregard the failure of the coupled inductor in the analysis. A solid foundation has been developed for system-level reliability analysis of the general  $N$ -phase topology. The derivation of the Markov reliability model to analyze the converter MTTF is described in the following.

## V. MARKOV RELIABILITY MODEL

Component failure rates are noted to be functions of operational conditions, such as number of phases, insolation, temperature, and device ratings. This precludes the possibility of using a combinatorial approach for reliability assessment [49]. Also, the failure-rate models are time invariant, and hence, do not capture time-varying stresses with diurnal and seasonal changes in insolation and temperature. One possible option is to design for worst case ambient conditions, while acknowledging the dependence of failure rates on converter topology. A Markov reliability model serves this method best, as state-dependent failure rates can easily be accommodated. In this section, a brief overview of Markov processes is given. State-transition diagrams and corresponding Chapman–Kolmogorov forward equations are subsequently derived and used to assess system reliability. For a more detailed treatment of the highlighted concepts, refer to [49].

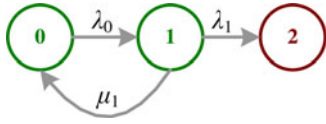


Fig. 17. Illustrative state-transition diagram.

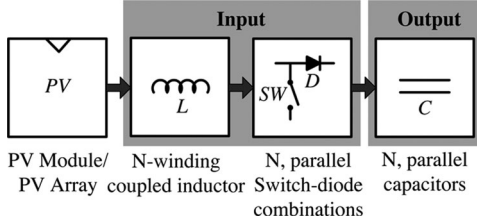


Fig. 18. Input and output stages highlighted.

### A. Preliminaries

A stochastic process  $X$  is defined as a collection of random variables  $\{x(t)\}$  indexed by a set  $T$ . For the Markov reliability model derived subsequently, the random variables represent possible converter topologies, and the index set is continuous time ( $t \geq 0$ ). If the stochastic process is described in continuous time and the random variables assume discrete values in a set  $S$ , the process is defined as a Markov process, if it satisfies the Markov property

$$\begin{aligned} & \Pr\{x(t_n)\} \\ &= s_n | \{x(t_{n-1}) = s_{n-1}, x(t_{n-2}) = s_{n-2}, \dots, x(t_0) = s_0\} \\ &= \Pr\{x(t_n) = s_n | x(t_{n-1}) = s_{n-1}\}. \end{aligned} \quad (28)$$

Continuous-time, time-homogenous Markov processes further satisfy the following property:

$$\begin{aligned} & \Pr\{X(t+s) = j | X(s) = i\} \\ &= \Pr\{X(t) = j | X(0) = i \forall s, t \geq 0\}. \end{aligned} \quad (29)$$

Markov reliability models can be graphically represented by the aid of state-transition diagrams. An example for a continuous-time, discrete-space Markov process is shown in Fig. 17. The nodes in the diagram represent the possible states that the Markov process may assume. For instance, consistent with the notation in (28), state zero represents  $x(t) = s_0$ , state one represents  $x(t) = s_1$ , and so on. Some transitions between the states are a consequence of faults (with failure rates  $\lambda_0$  and  $\lambda_1$ ). The process includes a repair transition from state  $s_1$  to  $s_0$  (with repair rate  $\mu_1$ ) that restores failed components. States with no outgoing transitions imply system failure and are referred to as absorbing states ( $s_2$ ). Nonabsorbing states are called transient states ( $s_0$  and  $s_1$ ).

For an  $N$ -phase converter, ideally, all phases and output capacitors are operational. However, the converter could function with a reduced number of phases and a depleted output capacitor bank. The failure of a switch, diode, or inductor in each phase would take that phase out of operation, but the capacitor bank could serve its fundamental purpose of energy storage with just one capacitor. As a matter of notation, the input stage

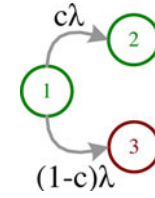
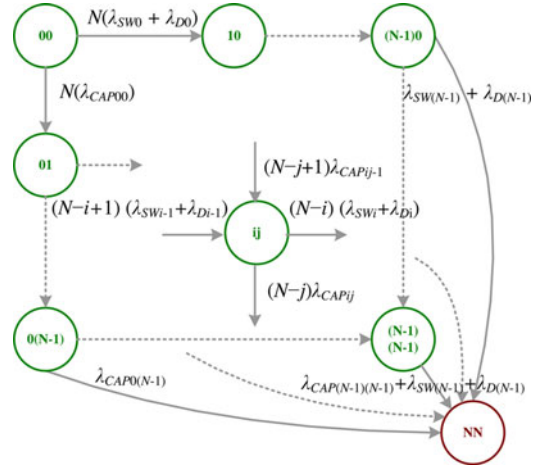


Fig. 19. Incorporating FDIR effectiveness using fault coverage.

Fig. 20. State-transition diagram of  $N$ -phase converter.

is composed of the inductors, switches, and diodes, and the output stage refers to the capacitor bank. This is depicted in Fig. 18. We presume that the controller is capable of fault detection, isolation, and reconfiguration (FDIR). Detection relates to making a binary decision whether or not a fault has occurred, isolation determines the location of the faulty component, and reconfiguration allows the converter to operate with a lower number of phases after the fault [50]. A metric commonly utilized to gauge the effectiveness of an FDIR controller is fault coverage. It is defined as the conditional probability that, given a fault has occurred, the system architecture is altered, and the intended functionality is restored [51]. Techniques to quantify fault coverage for dynamical systems of the kind considered in this paper are proposed in [52]. In essence, if detailed models are available, the FDIR effectiveness to handle each particular fault can be quantified by fault coverage  $c$ , which can be incorporated into the state-transition diagram, as shown in Fig. 19. As a consequence of a fault in State 1, a transition may be made to State 2 (fault detected and isolated) or to State 3 (failed state). Design and implementation aspects of FDIR are beyond the scope of this paper, and readers are referred to [50] and [52] and the references within for further information. In this study, we assume perfect FDIR, which implies  $c = 1$ . An advantage of the proposed framework is that it allows quantitative evaluation of the impact of different FDIR mechanisms on overall system reliability.

### B. State-Transition Diagrams

The state-transition diagram of an  $N$ -phase converter is shown in Fig. 20. The state  $ij$  represents an  $N$ -phase converter with  $i$



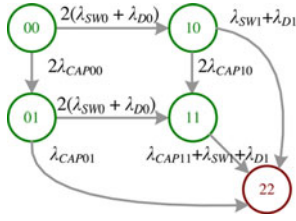


Fig. 21. State-transition diagram of two-phase converter.

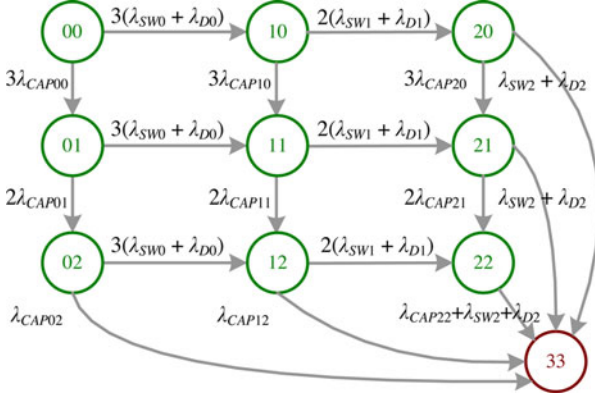


Fig. 22. State-transition diagram of three-phase converter.

failed input stages and  $j$  failed output stages. The failure rates of the switches and diodes in the converter are represented as  $\lambda_{SW/Dx}$ ,  $0 \leq x \leq N - 1$ , where  $x$  represents the number of failed input phases. The failure rates of the capacitors in the output stage are of the form  $\lambda_{CAPxy}$ ,  $0 \leq x \leq N - 1$ ,  $0 \leq y \leq N - 1$ . The first and second indices represent the number of failed input stages and failed output capacitors, respectively. Notice that the capacitor failure rates depend on the number of operational capacitors and the number of operational switching devices.

With reference to the state-transition diagram in Fig. 20, the failure rates corresponding to a transition from state  $ij$  to  $i(j+1)$  represent failures in the output stage (capacitor). The failure rate accompanying such a transition is of the form  $(N - j)\lambda_{CAPij}$ . Similarly, the failure rates corresponding to a transition from state  $ij$  to  $(i+1)j$  represent failure of an input stage (active switch or diode). The failure rate accompanying such a transition is of the form  $(N - i)(\lambda_{SWi} + \lambda_{Di})$ . Transitions from states of the general form  $(N - 1)j$  to state  $NN$  are at the rate  $(\lambda_{SWi} + \lambda_{Di})$ . Similarly, transitions from states of the general form  $i(N - 1)$  to state  $NN$  are at the rate  $\lambda_{CAPi(N-1)}$ . The state-transition diagrams of representative two- and three-phase converters are shown in Figs. 21 and 22, respectively.

### C. Chapman–Kolmogorov Forward Equations

The distribution of the Markov process at a given time  $t$  is expressed by the probability vector  $\mathbf{P}(t)$

$$\mathbf{P}(t) = [P_{00}(t), \dots, P_{ij}(t), \dots, P_{(N-1)(N-1)}(t)]. \quad (30)$$

The time evolution of the transition probabilities  $P_{ij}(t)$  is governed by the Kolmogorov forward equations [49]. For the  $N$ -

phase converter (see the state-transition diagram in Fig. 20), the following differential equations can be derived by inspection:

$$\frac{dP_{00}}{dt} = -N(\lambda_{SW0} + \lambda_{D0} + \lambda_{CAP00})P_{00}(t) \quad (31)$$

$$\begin{aligned} \frac{dP_{ij}}{dt} = & (N - j + 1)(\lambda_{CAPij-1})P_{ij-1}(t) - (N - j)(\lambda_{CAPij}) \\ & \times P_{ij}(t) + (N - i + 1)(\lambda_{SWi-1} + \lambda_{Di-1})P_{i-1j}(t) \\ & - (N - i)(\lambda_{SWi} + \lambda_{Di})P_{ij}(t). \end{aligned} \quad (32)$$

The Laplace transform of the Chapman–Kolmogorov equations are solved to quantify system reliability [49]. The Laplace transform of the transition probability of a given state  $ij$ ,  $P_{ij}^*(s)$  is computed as follows:

$$\begin{aligned} P_{ij}^*(s) = & \frac{(N - j + 1)(\lambda_{CAPi(j-1)})}{[s + (N - j)\lambda_{CAPij} + (N - i)(\lambda_{SWi} + \lambda_{Di})]} \\ & \times P_{i(j-1)}^*(s) \\ & + \frac{(N - i + 1)(\lambda_{SW(i-1)} + \lambda_{D(i-1)})}{[s + (N - j)\lambda_{CAPij} + (N - i)(\lambda_{SWi} + \lambda_{Di})]} \\ & \times P_{(i-1)j}^*(s). \end{aligned} \quad (33)$$

The Laplace transform of the transition probability of the operational state 00 can be expressed as follows:

$$P_{00}^*(s) = \frac{1}{[s + N(\lambda_{CAP00} + \lambda_{SW0} + \lambda_{D0})]}. \quad (34)$$

### D. Mean Time to System Failure

The overall system reliability is quantified using the MTTF. Since no repairs are included, the MTTF is more applicable as compared to the mean time between failures, which would typically find application in quantifying reliability of repairable systems. By definition, the mean time to system failure is expressed as follows:

$$\text{MTTF} = \int_{t=0}^{\infty} R(t)dt. \quad (35)$$

In the (35),  $R(t)$  denotes the reliability function of the system. The reliability function is expressed as the sum of the elements of the transition probability vector as follows:

$$R(t) = \sum_{i=0}^{N-1} \sum_{j=0}^{N-1} P_{ij}(t). \quad (36)$$

Taking the Laplace transform of both sides in (36) yields the following:

$$R^*(s) = \sum_{i=0}^{N-1} \sum_{j=0}^{N-1} P_{ij}^*(s). \quad (37)$$

The Laplace transform of the reliability function  $R^*(s)$  can be expressed as follows:

$$R^*(s) = \int_{t=0}^{\infty} R(t) \exp(-st)dt. \quad (38)$$

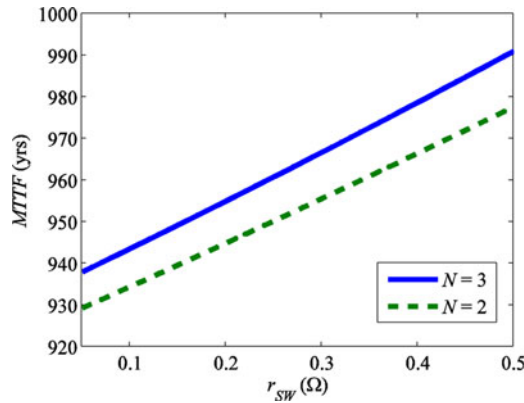


Fig. 23. MTTF as a function of switch resistance  $r_{SW}$ .

The MTTF can hence be determined as follows:

$$MTTF = \int_{t=0}^{\infty} R(t)dt = \int_{t=0}^{\infty} R(t) \exp(-0t)dt = R^*(0). \quad (39)$$

In essence, (39) suggests that MTTF can be found simply from the Laplace transform of the reliability function as follows:

$$MTTF = \sum_{i=0}^{N-1} \sum_{j=0}^{N-1} P_{ij}^*(0). \quad (40)$$

### E. Case Studies

The applicability of the derived Markov reliability model is demonstrated in the context of comparative studies for two- and three-phase, interleaved boost converters. The converter specifications and device ratings are documented in Table II. The variation of the MTTF for two- and three-phase converters as a function of switch resistance  $r_{SW}$  is depicted in Fig. 23. Surprisingly, an increase in  $r_{SW}$  increases the MTTF. This is because, for a fixed resistive load, an increase in  $r_{SW}$  reduces the output voltage. Assuming that the ambient temperature remains unchanged, the stress on the output capacitors is reduced, making them more reliable. Since the capacitors dominate the reliability of the converter, the MTTF is increased.

A cursory comparison of the failure rates illustrated in Figs. 13–16 indicates that the capacitor failure rates are higher than those of the switches across all ambient conditions and design choices. Hence, the overall converter reliability is expected to be dominated by the output capacitors. Toward this end, the impact of the voltage rating of the capacitors  $V_{RATING-CAP}$  on the MTTF of two- and three-phase converters is considered. As Fig. 24 indicates, the MTTF is much more sensitive to  $V_{RATING-CAP}$  than  $r_{SW}$ .

Fig. 25 illustrates the impact of the choice of capacitance on the MTTF of two- and three-phase converters. For a fair comparison, the capacitors in the two-phase converter are rated for 110 V, while those in the three-phase converter are rated for 100 V. This ensures that the MTTF of the two converters is almost the same for the base-case specifications attached in Table II. The results illustrate that for each converter, there is an optimal capacitance value that maximizes the MTTF. Also,

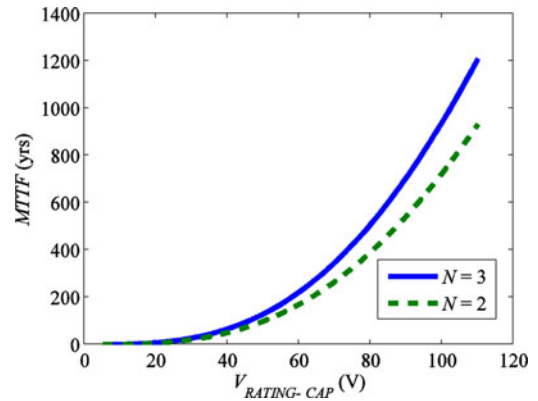


Fig. 24. MTTF as a function of capacitor voltage rating  $V_{RATED-CAP}$ .

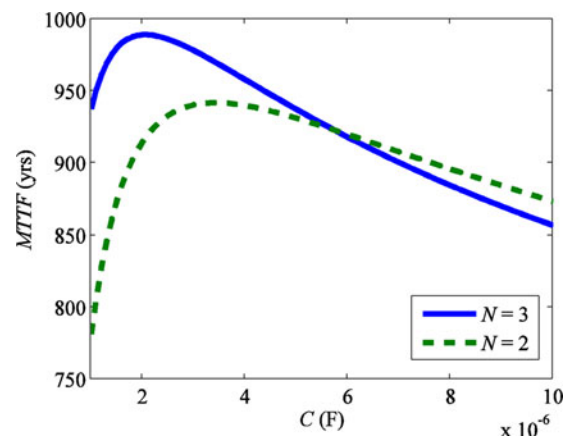


Fig. 25. MTTF as a function of capacitance  $C$ .

note that topological redundancy does not necessarily improve reliability. For capacitances below  $6 \mu\text{F}$ , the voltage stress tends to dominate  $\lambda_{CAP}$ , and a higher number of phases guarantee improved reliability. Beyond  $6 \mu\text{F}$ , the degradation in the failure rate due to high capacitance and the higher voltage rating of the capacitors in the two-phase converter overshadow the voltage stress factor, making the two-phase converter more reliable.

Finally, the impact of switching frequency on the MTTF is shown in Fig. 26. The only switching-frequency-dependent parameter in the steady-state analysis is the output voltage ripple (19) that affects the capacitor failure rate (24). Increasing the switching frequency improves capacitor reliability as voltage ripple is reduced. Since the capacitors dominate system reliability, reductions in their failure rate translate to dramatic improvements in system MTTF. However, including frequency-dependent losses in the analysis (e.g., switching loss and hysteresis loss) would reduce the MTTF at high switching frequencies. The comparison of the two- and three-phase converter MTTF shown in Fig. 26 also indicates that the three-phase converter is more reliable only up to a switching frequency of 12 kHz. Beyond that, the higher voltage rating of the capacitors in the two-phase converter allows this topology to be more reliable across all possible switching frequencies.

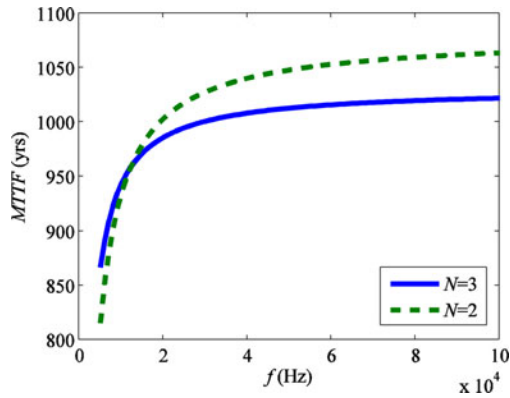


Fig. 26. MTTF as a function of switching frequency  $f_{SW}$ .

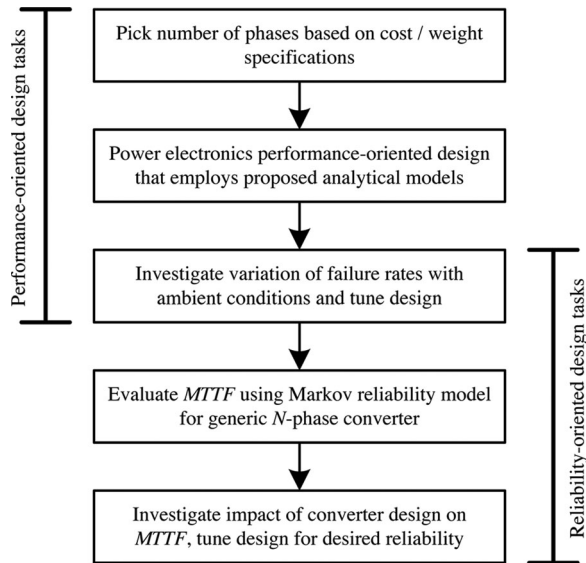


Fig. 27. Suggested design practice to integrate reliability into performance-based design

## VI. CONCLUSION

A comprehensive design procedure that integrates performance and reliability metrics is suggested for topologically redundant switch-mode power converters in PV energy conversion applications. The analysis begins with a detailed description of the steady-state operation of a candidate multiphase boost converter topology. The analytical description of the converter provides expressions to rapidly quantify the operational stresses on the components. Then, the variation of device failure rates is analyzed across a wide range of representative ambient conditions and converter design choices. Finally, a Markov reliability model of a generic  $N$ -phase converter that enables the evaluation of system reliability metrics, such as MTTF, is derived.

The proposed approach to integrating reliability in performance-based design for power converters naturally lends itself to design procedures that can be adopted by practicing engineers. Design choices such as the choice of capacitor technology, switch ratings, and device parasitics not only have an impact on cost and performance, but also influence system reliability. This framework provides a unified methodology to

explore these links and the impact of various design choices. An illustrative design strategy is shown in Fig. 27. Notice the significant overlap in design tasks, which conventionally would be construed as related to either reliability assessment or performance-oriented design.

Future research may investigate the application of time-varying failure rates. In addition, numerical optimization tools could suggest optimal converter specifications, given bounds on performance, reliability, cost, and weight. More accurate thermal models could be used to specify the device failure rates. Detailed models to quantify the copper and core loss in the inductors, and switching and commutation losses in the active and passive switches could be included. Reliability of switch drivers, operational amplifiers, and microcontrollers could also be modeled in the framework. Including these details will increase analytical complexity, but will yield lower MTTF numbers, likely to be seen in the field, once the converters are deployed. Similar tools could also be employed to specify the reliability of other power electronic converters, such as inverters and rectifiers.

## APPENDIX A

TABLE I  
PARAMETERS OF PV MODULE: SPR-230-WHT [36]

Symbol	Quantity	Value
$V_{OC-STC}$	Rated open-circuit voltage	48.7 V
$I_{SC-STC}$	Rated short-circuit current	5.99 A
$I_{M-STC}$	Rated current	5.61 A
$V_{M-STC}$	Rated voltage	41 V
$\alpha$	Temperature coefficient for current	3.5 mA / °C
$\beta$	Temperature coefficient for voltage	132.5 mV / °C

## APPENDIX B

TABLE II  
COMPONENT CHOICES AND RATINGS

Symbol	Quantity	Value
$L$	Self inductance of coupled inductor	1.2 mH
$M$	Mutual inductance of coupled inductor	1.18 mH
$r_L$	Winding resistance of each phase	0.1 $\Omega$
$r_{SW}$	Drain-source on-state switch resistance	0.1 $\Omega$
$V_f$	Forward voltage drop of diode	1 V
$C$	Output capacitance	4.7 $\mu$ F
$R$	Output load	50 $\Omega$
$f$	Switching frequency	10 kHz
$P_{RATING-SW}$	Power rating of active switches	200 W
$V_{RATING-DIODE}$	Voltage rating of diode	150 V
$\Theta_{JC}$	Junction-case thermal resistance	5 °C/W
$V_{RATING-CAP}$	Voltage rating of capacitor	100 V

## REFERENCES

- [1] F. Liccardo, P. Marino, G. Torre, and M. Triggianese, "Interleaved dc-dc converters for photovoltaic modules," in *Proc. Int. Conf. Clean Elect. Power*, 2007, pp. 201–207.
- [2] J.-P. Lee, B.-D. Min, T.-J. Kim, D.-W. Yoo, and J.-Y. Yoo, "A novel topology for photovoltaic Dc/Dc full-bridge converter with flat efficiency under wide PV module voltage and load range," *IEEE Trans. Ind. Electron.*, vol. 55, no. 7, pp. 2655–2673, Jul. 2008.
- [3] P. Wong, P. Xu, B. Yang, and F. C. Lee, "Performance improvements of interleaving VRMs with coupling inductors," *IEEE Trans. Power Electron.*, vol. 16, no. 4, pp. 499–507, Jul. 2001.

- [4] J. Sun, Y. Qiu, M. Xu, and F. C. Lee, "High-frequency dynamic current sharing analyses for multiphase buck VRs," *IEEE Trans. Power Electron.*, vol. 22, no. 6, pp. 2424–2431, Nov. 2007.
- [5] T. Carosa, R. Zane, and D. Maksimovic, "Scalable digital multiphase modulator," *IEEE Trans. Power Electron.*, vol. 23, no. 4, pp. 2201–2205, Jul. 2008.
- [6] K. Jin, M. Xu, Y. Sun, D. Sterk, and F. C. Lee, "Evaluation of self-driven schemes for a 12-V self-driven voltage regulator," *IEEE Trans. Power Electron.*, vol. 24, no. 10, pp. 2314–2322, Oct. 2009.
- [7] K. Lee, F. C. Lee, and M. Xu, "A hysteretic control method for multiphase voltage regulator," *IEEE Trans. Power Electron.*, vol. 24, no. 12, pp. 2726–2734, Dec. 2009.
- [8] S. Dwari and L. Parsa, "A novel high efficiency high power interleaved coupled-inductor boost dc-dc converter for hybrid and fuel cell electric vehicle," in *Proc. Vehicle Power Propul. Conf.*, Oct. 2007, pp. 309–404.
- [9] X. Xu, W. Liu, and A. Q. Huang, "Two-phase interleaved critical mode pfc boost converter with closed loop interleaving strategy," *IEEE Trans. Power Electron.*, vol. 24, no. 12, pp. 3003–3013, Dec. 2009.
- [10] C. Chang and M. A. Knights, "Interleaving technique in distributed power conversion systems," *IEEE Trans. Circuits Syst. I, Fundam. Theory Appl.*, vol. 42, no. 5, pp. 245–251, May 1995.
- [11] M. Veerachary, T. Senjyu, and K. Uezato, "Maximum power point tracking of coupled inductor interleaved boost converter supplied PV system," *Proc. Inst. Elect. Eng., Elect. Power Appl.*, vol. 150, no. 1, pp. 71–80, Jan. 2003.
- [12] P.-W. Lee, Y.-S. Lee, D. K. W. Cheng, and X.-C. Liu, "Steady-state analysis of an interleaved boost converter with coupled inductors," *IEEE Trans. Ind. Electron.*, vol. 47, no. 4, pp. 787–795, Aug. 2000.
- [13] R. Leyva, C. Alonso, I. Queinnec, A. Cid-Pastor, D. Lagrange, and L. Martinez-Salamero, "MPPT of photovoltaic systems using extremum—Seeking control," *IEEE Aerospace Electron. Syst.*, vol. 42, no. 1, pp. 249–258, Jan. 2006.
- [14] C. Cabal, A. Cid-Pastor, L. Seguier, B. Estibals, and C. Alonso, "Improved photovoltaic conversion chain with interleaved method," in *Proc. IEEE Power Electron. Spec. Conf.*, 2008, pp. 70–75.
- [15] H.-B. Shin, J.-G. Park, S.-K. Chung, H.-W. Lee, and T. A. Lipo, "Generalized steady-state analysis of multiphase interleaved boost converter with coupled inductors," *Proc. Inst. Elect. Eng., Elect. Power Appl.*, vol. 152, no. 3, pp. 584–594, May 2005.
- [16] H.-B. Shin, E.-S. Jang, J.-G. Park, H.-W. Lee, and T. A. Lipo, "Small-signal analysis of multiphase interleaved boost converter with coupled inductors," *Proc. Inst. Elect. Eng., Elect. Power Appl.*, vol. 152, no. 5, pp. 1161–1170, Sep. 2005.
- [17] E. L. Meyer and E. E. van Dyk, "Assessing the reliability and degradation of photovoltaic module performance parameters," *IEEE Trans. Rel.*, vol. 53, no. 1, pp. 83–92, Mar. 2004.
- [18] M. Vazquez and I. R. -Stolle, "PV module reliability model based on field-degradation studies," *Prog. Photovoltaic: Res. Appl.*, vol. 16, pp. 419–433, 2008.
- [19] G. Petrone, G. Spagnuolo, R. Teodorescu, M. Veerachary, and M. Vitelli, "Reliability issues in photovoltaic power processing systems," *IEEE Trans. Ind. Electron.*, vol. 55, no. 7, pp. 2569–2580, Jul. 2008.
- [20] N. G. Dhere, "Reliability of PV modules and balance-of-system components," in *Proc. IEEE Photovolt. Spec. Conf.*, 2005, pp. 1570–1576.
- [21] A. Ristow, M. Begovic, A. Pregelj, and A. Rohatgi, "Development of a methodology for improving photovoltaic inverter reliability," *IEEE Trans. Ind. Electron.*, vol. 55, no. 7, pp. 2581–2592, Jul. 2008.
- [22] H. Calleja, F. Chan, and I. Uribe, "Reliability-oriented assessment of a Dc/Dc converter for photovoltaic applications," in *Proc. IEEE Power Electron. Spec. Conf.*, 2007, pp. 1522–1527.
- [23] F. Chan, H. Calleja, and E. Martinez, "Grid connected PV systems: A reliability-based comparison," in *Proc. IEEE Int. Symp. Ind. Electron.*, 2006, pp. 1583–1588.
- [24] F. Chan and H. Calleja, "Reliability: A new approach in design of inverters for PV systems," in *Proc. IEEE Int. Power Electron. Congr.*, 2006, pp. 1–6.
- [25] Q. Li and P. Wolfs, "A review of the single phase photovoltaic module integrated converter topologies with three different dc link configurations," *IEEE Trans. Power Electron.*, vol. 23, no. 3, pp. 1320–1333, May 2008.
- [26] T. Kerekes, R. Teodorescu, M. Liserre, C. Klumpner, and M. Sumner, "Evaluation of three-phase transformerless photovoltaic inverter topologies," *IEEE Trans. Power Electron.*, vol. 24, no. 9, pp. 2202–2211, Sep. 2009.
- [27] S. B. Kjaer, J. K. Pederson, and F. Blaabjerg, "A review of single-phase grid-connected inverters for photovoltaic modules," *IEEE Trans. Power Electron.*, vol. 41, no. 5, pp. 1292–1306, Oct. 2005.
- [28] Y. C. Qin, N. Mohan, R. West, and R. Bonn. (2002, Jun.). Status and needs of power electronics for photovoltaic inverters. Sandia National Labs., New Mexico. [Online]. Available: <http://www.prod.sandia.gov/cgi-bin/techlib/access-control.pl/2002/021535.pdf>.
- [29] F. Chan and H. Calleja, "Design strategy to optimize the reliability of grid-connected PV systems," *IEEE Trans. Ind. Electron.*, vol. 56, no. 11, pp. 4465–4472, Nov. 2009.
- [30] S. V. Dhople, A. Davoudi, and P. L. Chapman, "Steady-state characterization of multiphase, interleaved dc-dc converters for photovoltaic applications," in *Proc. IEEE Energy Convers. Congr. Expo.*, 2009, pp. 330–336.
- [31] S. V. Dhople, A. Davoudi, P. L. Chapman, and A. D. Domínguez-García, "Reliability assessment of fault tolerant dc-dc converters for photovoltaic applications," in *Proc. IEEE Energy Convers. Congr. Expo.*, 2009, pp. 2271–2276.
- [32] J. A. Gow and C. D. Manning, "Development of a photovoltaic array model for use in power-electronics simulation studies," *Proc. Inst. Elect. Eng. Elect. Power Appl.*, vol. 146, no. 2, pp. 193–200, Mar. 1999.
- [33] M. S. Suresh, "Measurement of solar cell parameters using impedance spectroscopy," *Solar Energy Mater. Solar Cells*, vol. 43, pp. 21–28, Aug. 1996.
- [34] D. S. H. Chan, J. R. Phillips, and J. C. H. Phang, "A comparative study of extraction methods for solar cell model parameters," *Solid-State Electron.*, vol. 29, no. 3, pp. 329–337, Mar. 1986.
- [35] S. Jianhui, Y. Shijie, and Z. Wei, "Investigation on engineering analytical model of silicon solar cell," in *Acta Energiæ Solaris Sinica*, 2001, pp. 409–412.
- [36] SPR-230-WHT, Sunpower 230 Watt PV Module data sheet. (2007, Oct.) [Online]. Available: <http://www.sunpowercorp.com>
- [37] A. Pandey, N. Dasgupta, and A. K. Mukerjee, "A simple single-sensor MPPT solution," *IEEE Trans. Power Electron.*, vol. 22, no. 2, pp. 698–700, Mar. 2007.
- [38] N. Femia, G. Petrone, G. Spagnuolo, and M. Vitelli, "Optimization of perturbation and observe maximum power point tracking method," *IEEE Trans. Power Electron.*, vol. 20, no. 4, pp. 963–973, Jul. 2005.
- [39] K. K. Tse, M. T. Ho, H. S. Chung, and S. Y. Hui, "A novel maximum power point tracker for PV panels using switching frequency modulation," *IEEE Trans. Power Electron.*, vol. 17, no. 4, pp. 980–989, Nov. 2002.
- [40] E. V. Solodovnik, L. Shengyi, and R. A. Dougal, "Power controller design for maximum power tracking in solar installations," *IEEE Trans. Power Electron.*, vol. 19, no. 5, pp. 1295–1304, Sep. 2004.
- [41] T. Eram, J. W. Kimball, P. T. Krein, P. L. Chapman, and P. Midya, "Dynamic maximum power point tracking of photovoltaic arrays using ripple correlation control," *IEEE Trans. Power Electron.*, vol. 21, no. 5, pp. 1282–1291, Sep. 2006.
- [42] J. W. Kimball and P. T. Krein, "Discrete-time ripple correlation control for maximum power point tracking," *IEEE Trans. Power Electron.*, vol. 23, no. 5, pp. 2353–2362, Sep. 2008.
- [43] G. Eirea and S. R. Sanders, "Phase current unbalance estimation in multiphase buck converters," *IEEE Trans. Power Electron.*, vol. 23, no. 1, pp. 137–143, Jan. 2008.
- [44] J. A. A. Qahouq, L. Huang, and D. Huard, "Sensorless current sharing analysis and scheme for multiphase converters," *IEEE Trans. Power Electron.*, vol. 23, no. 5, pp. 2237–2247, Sep. 2008.
- [45] O. Garcia, P. Zumel, A. de Castro, P. Alou, and J. A. Cobos, "Current self-balance mechanism in multiphase buck converter," *IEEE Trans. Power Electronics*, vol. 24, pp. 1600–1606, Jun. 2009.
- [46] MIL-HDBK-217F—*Military Handbook for Reliability Prediction of Electronic Equipment*, Department of Defense, Washington, DC, Jan. 1990.
- [47] M. Held and K. Fritz, "Comparison and evaluation of newest failure rate prediction models: FIDES and RIAC 217PLUS," *Microelectron. Rel.*, vol. 49, pp. 967–971, Sep. 2009.
- [48] G. Chen, R. Burgos, Z. Liang, F. Wang, J. D. van Wyk, W. G. Odendaal, and D. Boroyevich, "Reliability-oriented design considerations for high-power converter modules," in *Proc. IEEE Power Electron. Spec. Conf.*, 2004, pp. 419–425.
- [49] M. Rausand and A. Høyland, *System Reliability Theory*. Hoboken, NJ: Wiley, 2004.
- [50] K. Levin, E. M. Hope, and A. D. Domínguez-García, "Observer-based fault diagnosis of power electronics systems," in *Proc. IEEE Energy Convers. Congr. Expo.*, 2009, pp. 4434–4440.
- [51] A. D. Domínguez-García and P. T. Krein, "Integrating reliability into the design of fault-tolerant power electronics systems," in *Proc. IEEE Power Electron. Spec. Conf.*, 2008, pp. 2665–2671.
- [52] A. D. Domínguez-García, J. G. Kassakian, and J. E. Schindall, "A generalized fault coverage model for linear time-invariant systems," *IEEE Trans. Rel.*, vol. 58, no. 3, pp. 553–567, Sep. 2009.



**Sairaj V. Dhople** (S'09) received the B.S. and M.S. degrees in electrical engineering, in 2007 and 2009, respectively, from the University of Illinois, Urbana-Champaign, where he is currently working toward the Ph.D. degree.

His research has been concerned with the reliability and optimal control of dc–dc converters for photovoltaic energy-conversion applications.



**Alejandro D. Domínguez-García** (M'07) received the M.S. degree in electrical engineering from the University of Oviedo, Spain, in 2001, and the Ph.D. degree in electrical engineering and computer science from the Massachusetts Institute of Technology, Cambridge, in 2007.

He was a Postdoctoral Research Associate at the Laboratory for Electromagnetic and Electronic Systems, Massachusetts Institute of Technology. He is currently an Assistant Professor in the Electrical and Computer Engineering Department, University of Illinois, Urbana, where he is affiliated with the power and energy systems area. His research interests include system reliability theory and control, and their applications to electric power systems, power electronics, and embedded electronic systems for safety-critical/fault-tolerant aircraft, aerospace, and automotive applications.

Dr. Domínguez-García received the National Science Foundation (NSF) CAREER Award in 2010.



**Ali Davoudi** (S'04–M'11) received the B.Sc. degree from Sharif University of Technology, Tehran, Iran, in 2003, the M.Sc. degree from The University of British Columbia, Vancouver, BC, Canada, in 2005, and the Ph.D. degree from the University of Illinois, Urbana, in 2010, all in electrical and computer engineering.

He was a Visiting Scholar at The University of British Columbia and a Visiting Lecturer and a Postdoctoral Research Associate at The University of Illinois. He was also engaged at Solar Bridge Technologies, Texas Instruments Inc., and Royal Philips Electronics. He is currently an Assistant Professor at the Department of Electrical Engineering, University of Texas, Arlington. His research interests include all aspects of modeling, simulation, and control of power electronics and energy conversion systems, renewable energy sources, and transportation electrification.

Dr. Davoudi is an Associate Editor for the IEEE TRANSACTIONS ON VEHICULAR TECHNOLOGY.



**Patrick L. Chapman** (S'94–M'00–SM'05) received the B.S. and M.S. degrees in electrical engineering from the University of Missouri-Rolla, Rolla, in 1996 and 1997, respectively, and the Ph.D. degree from Purdue University, West Lafayette, IN, in 2000.

He was a Willett Faculty Scholar, Grainger Associate, and Associate Professor at the University of Illinois, Urbana-Champaign. He is currently a Cofounder and the Chief Technology Officer of SolarBridge Technologies, Inc. His research interests within power electronics include applications to

integrated design, renewable energy, electromechanics, automated modeling, hybrid energy systems, and energy harvesting.

Dr. Chapman is an Editor for the IEEE TRANSACTIONS ON ENERGY CONVERSION, and a Historian for the IEEE Power Electronics Society (PELS). He is a Member-at-Large for the IEEE PELS Administrative Committee, and is currently the General Chair for the 2011 IEEE APEC. He has received the National Science Foundation (NSF) CAREER Award and the Office of Naval Research Young Investigator Award. He was named the Richard M. Bass Outstanding Young Power Electronics Engineer in 2006.